

Broadband Photoresponse Arising from Photo-Bolometric Effect in Quasi-One-Dimensional Ta₂Ni₃Se₈

W L Zhen^{1,2}, W T Miao¹, W L Zhu¹, C J Zhang^{1,3,*} and W K Zhu^{1,*}

¹ High Magnetic Field Laboratory, Chinese Academy of Sciences, Hefei 230031, People's Republic of China

² University of Science and Technology of China, Hefei 230026, People's Republic of China

³ Institutes of Physical Science and Information Technology, Anhui University, Hefei 230601, People's Republic of China

E-mail: zhangcj@hmfl.ac.cn and wkzhu@hmfl.ac.cn

Abstract

In this paper, we report the synthesis of high-quality Ta₂Ni₃Se₈ crystals free of noble or toxic elements and the fabrication and testing of photodetectors on the wire samples. A broadband photoresponse from 405 nm to 1550 nm is observed, along with performance parameters including relatively high photoresponsivity (10 mA W⁻¹) and specific detectivity (3.5×10^7 Jones) and comparably short response time ($\tau_{\text{rise}} = 433$ ms, $\tau_{\text{decay}} = 372$ ms) for 1064 nm, 0.5 V bias and 1.352 mW mm⁻². Through extensive measurement and analysis, it is determined that the dominant mechanism for photocurrent generation is the photo-bolometric effect, which is believed to be responsible for the very broad spectral detection capability. More importantly, the pronounced response to 1310 nm and 1550 nm wavelengths manifests its promising applications in optical communications. Considering the quasi-one-dimensional structure with layered texture, the potential to build nanodevices on Ta₂Ni₃Se₈ makes it even more important in future electronic and optoelectronic applications.

Keywords: narrow bandgap semiconductors, optoelectronic devices, infrared detectors, optical communications

1. Introduction

Photodetectors, with the ability to convert incident light into electrical signals, are essential for industrial and scientific applications [1-3]. Generally, photodetectors can be divided into two types, i.e., specific wavelength detectors (ultraviolet (UV) detectors, visible light (vis) detectors or infrared (IR) detectors) and broadband detectors (UV-IR detectors) [4], according to the detection spectral range. Specific wavelength photodetectors need to work under a certain single wavelength or a narrow range of light, showing specific applications in light detection and nanophotonic integrated circuits [5, 6]. In contrast, broadband photodetectors have enormous potential applications in UV-vis-IR light communications, memory storage and broad-spectrum switching in a single optoelectronic system [1, 7, 8]. In the past few years, many commercial photodetectors are typically based on crystalline GaN [9], Si [10] and InGaAs [11] and used for 250–400 nm (UV), 400–800 nm (vis) and 900–1700 nm (near-IR) detection, respectively. In addition, longwave IR detectors based on narrow bandgap or semimetal materials have been extensively studied, such as HgCdTe [12], InSb [13, 14] and Cd₃As₂ [15]. Although these materials show good performance in the near-IR and longwave IR, photodetectors based on these materials contain toxic elements and often require low temperatures to achieve high performance, which makes the systems bulky, expensive, and harmful to humans and the environment [16]. Therefore, there is a great need to develop high-performance IR photodetectors that operate at room temperature and consist only of low-cost and nontoxic elements.

Recently, the quasi-one-dimensional (quasi-1D) chain compounds M₂X₃Y₈ (M= Ta, Nb; X= Ni, Pd, Pt; Y=S, Se) have drawn considerable attention for their intriguing electronic properties related to the quasi-1D structure [17-20]. For the crystal structure, the atoms in the chains are connected by strong chemical bonds, while the inter-chain bonds are relatively weak, i.e., the van-der-Waals (vdW) interactions. Crystals of this type usually show a needle-like or fine hair morphology. For the electronic structure, the Ta₂Pd₃Se₈ and

Ta₂Pt₃Se₈ transistors are n-type and p-type semiconductors, respectively [18]. Meanwhile, these materials also exhibit outstanding optoelectronic properties [21, 22]. Among these compounds, Ta₂Ni₃Se₈ is a low-cost material free of noble or toxic elements, unlike its analogues with noble metals such as Pd and Pt. Ta₂Ni₃Se₈ nanowire transistor has been identified as an ambipolar semiconductor [20]. Considering the interesting electronic structure and properties, Ta₂Ni₃Se₈ holds promise for possible applications in the field of photodetection, but it remains to be explored.

In this work, we report the synthesis of high-quality Ta₂Ni₃Se₈ crystals and the fabrication and testing of photodetectors on the wire samples. A broadband photoresponse from 405 nm to 1550 nm is observed, along with performance parameters including relatively high photoresponsivity (10 mA W⁻¹) and specific detectivity (3.5×10^7 Jones) and comparably short response time ($\tau_{\text{rise}} = 433$ ms, $\tau_{\text{decay}} = 372$ ms) for 1064 nm, 0.5 V bias and 1.352 mW mm⁻². Through extensive measurement and analysis, it is determined that the dominant mechanism for photocurrent generation is the photo-bolometric (PB) effect, which is believed to be responsible for the very broad spectral detection capability. More importantly, the pronounced response to 1310 nm and 1550 nm wavelengths manifests its promising applications in optical communications. The quasi-1D structure with layered texture and the potential to build nanodevices make it even more important.

2. Methods

Ta₂Ni₃Se₈ crystals were prepared by a one-step method [20]. High purity powders of Ta (99.98%, Alfa Aesar), Ni (99.9%, Alfa Aesar) and Se (99.9%, Alfa Aesar) were mixed and ground in a chemical molar ratio of 2:3:10. The mixture was then sealed in a 12 cm long evacuated quartz ampule, heated to 700 °C at a rate of 2 °C/min, and kept at this temperature for 7 days before cooling down to room temperature. After the reaction, large needle-like or fine hair-like Ta₂Ni₃Se₈ crystals can be obtained on the surface of the solid solution. See the supplementary information for the optical image. The crystal structure and phase purity were checked by X-ray diffraction (XRD) analysis on a Rigaku-TTR3 X-

ray diffractometer using Cu $K\alpha$ radiation at room temperature. Chemical composition characterization was performed on an Oxford Inca energy dispersive spectrometer (EDS) equipped with a FEI Helios Nanolab 600i scanning electron microscope (SEM). Raman spectrum was collected in a backscattering geometry on a Horiba JobinYvon T6400 spectrometer with a 532 nm laser.

Photodetectors were fabricated based on $Ta_2Ni_3Se_8$ wires. Gold wires were directly connected to the sample using silver paste for good ohmic contact. According to the previous reference [20], the use of chromium as the contact electrodes resulted in a relatively low Schottky barrier of 50 meV, which was a nearly ohmic contact. Considering the low work function of chromium (4.5 eV) and the ambipolar semiconductor characteristic of $Ta_2Ni_3Se_8$, we adopted another low work function metal, i.e., silver (4.3 eV). The channel area of the device on SiO_2 (300 nm)/Si substrate was about $1 \mu m \times 2 mm$, and the thickness of the active material was about 2 μm . The optoelectronic measurements were carried out on a home-built multi measurement system consisting of a microscope, a four-probe station, a semiconductor parameter analyzer (2636B, Keithley) and laser light sources with different wavelengths. The incident light power density was measured using a power meter (PM100D, Thorlabs). The incident laser spot diameter was approximately 5 mm, which is larger than the channel area to ensure uniform illumination. The electronic structure of bulk $Ta_2Ni_3Se_8$ was theoretically investigated by first-principles calculations using the WIEN2K code [23]. The generalized gradient approximation (GGA) of Perdew-Burke-Ernzerhof [24] was employed with a k -mesh of 1000 points. The lattice constants used for the calculations were taken from the Springer Materials website.

3. Results and discussion

The crystal structure of $Ta_2Ni_3Se_8$ is orthorhombic with the space group $Pbam$. It is found that the unit cell of $Ta_2Ni_3Se_8$ contains four interconnected chains forming a zigzag structure extending along the c -axis. Each chain consists of two edge-sharing chains of trigonal prisms centered on Ta atoms and bridged by Ni atoms, as shown in figure 1(a).

Between linear chains are vdW gaps, which facilitate the quasi-1D structure. Figures 1(b) and (c) show the band structure and density of states (DOS) of $\text{Ta}_2\text{Ni}_3\text{Se}_8$ along the high symmetry directions, respectively. The calculated bandgap is about 0.25 eV, indicating that it is a narrow bandgap semiconductor. The obtained value is close to the reported results [20], confirming the reliability of our calculations. From the band structure, the bandgap is an indirect one since the valence band maximum (VBM) and conduction band minimum (CBM) do not coincide at the same point. The VBM and CBM appear to be in the UX and YZ segments, respectively. From the DOS plots, the CBM and VBM are mainly composed of distorted *d* and *p* orbitals of Ta, Ni and Se ions, revealing the nature of covalent bonding.

The obtained crystals were characterized by XRD, EDS and Raman spectroscopy. Figure 2(a) shows the XRD pattern of a bunch of thin wires. All diffraction peaks can be indexed, which is in good agreement with the powder XRD results (JCPDS PDF No. 00-086-0186), indicating that the compound is single-phase $\text{Ta}_2\text{Ni}_3\text{Se}_8$. Figure 2(b) shows a typical SEM image of a $\text{Ta}_2\text{Ni}_3\text{Se}_8$ wire. The surface of the wire is flat and smooth. Interestingly, the side view reveals a feature of layered texture, suggesting the possibility of exfoliation. The EDS spectrum collected on the wire surface indicates a chemical composition of Ta:Ni:Se = 16.44%:23.62%:59.94% (figure 2(c)), which is very close to the stoichiometric ratio of 2:3:8. Note that due to the low melting point (221°C) and high saturation vapor pressure of Se, there is a certain degree of Se vacancies. Furthermore, figure 2(d) shows the EDS mapping results of the total scan and elemental scan of Ta, Ni and Se atoms, respectively. The uniform distribution of the elements confirms the high quality of the crystals. More EDS data are presented in the supplementary information. In addition, the Raman spectrum shown in the supplementary information is consistent with a recent report [25]. No photoluminescence signal was observed due to the indirect bandgap feature.

To investigate the optoelectronic properties of $\text{Ta}_2\text{Ni}_3\text{Se}_8$, several two-terminal devices with similar dimensions were fabricated based on $\text{Ta}_2\text{Ni}_3\text{Se}_8$ wires and tested. Since there

are no significant differences between these devices, we only provide experimental results for a representative device here (see the supplementary information for other devices). In figure 3, we summarize the optoelectronic measurements of device D1 in the dark and under laser illumination of different wavelengths (λ), i.e., 405 nm, 450 nm, 488 nm, 635 nm, 780 nm, 830 nm, 940 nm and 1064 nm. The laser power density is tuned to a constant value of 1.352 mW mm^{-2} . As shown in figure 3(a), the current-voltage (I - V) characteristic curves pass through the origin and are almost completely linear with $\pm 0.5 \text{ V}$, indicating a good ohmic contact between $\text{Ta}_2\text{Ni}_3\text{Se}_8$ and the electrodes, which also rules out the possibility of Schottky contact. The inset shows an enlarged view of the I - V curves in the range of 0.48 V to 0.5 V . The dark current at 0.5 V corresponds to a current density of 256 A cm^{-2} . A clear difference between the dark and illuminated states is observed at all laser wavelengths, implying that the photodetector responds to a broad spectral range from UVA to the entire visible spectrum to the near-IR. Figure 3(b) shows the calculated photocurrents for various wavelengths under 0.5 V bias. The photocurrent is defined as $I_{\text{ph}} = I_{\text{illumination}} - I_{\text{dark}}$, where $I_{\text{illumination}}$ and I_{dark} are the currents measured in the illuminated and dark states, respectively. From figure 3(b), the photocurrent at $\lambda = 405 \text{ nm}$ is remarkable, reaching 120 nA . Although it degrades for longer wavelengths, the photocurrent in the IR region is significant enough. Given that the calculated bandgap of $\text{Ta}_2\text{Ni}_3\text{Se}_8$ is 0.25 V , which corresponds to a wavelength of 4959 nm , the wavelengths used in the present work far exceed the bandgap. Shorter wavelength photons have higher energy and will excite more electrons deep in the valence band [26]. This could explain the phenomenon that larger photocurrents appear at shorter wavelength. This is a preliminary judgement. In-depth studies on the mechanism will be presented in the next section.

To further evaluate the optoelectronic performance, some key parameters are calculated, including responsivity ($R = \frac{I_{\text{ph}}}{PS}$, where P is the laser power density and S is the illuminated area) representing the conversion efficiency from incident light signal to electrical signal, specific detectivity ($D^* = R \sqrt{\frac{S}{2eI_{\text{dark}}}}$, where e is the elementary charge)

characterizing the capability to detect the lowest light signal, and external quantum efficiency ($\text{EQE} = \frac{hc}{e\lambda}R \times 100\%$, where c is the speed of light in vacuum) referring to the number of electrons excited by each incident photon [27, 28]. Figures 3(c) and (d) show R (left axis), D^* (right) and EQE as a function of wavelength, respectively. The most significant parameters are recorded as $R = 43.3 \text{ mA W}^{-1}$, $D^* = 1.5 \times 10^8 \text{ Jones}$ and $\text{EQE} = 13.3\%$, appearing at $\lambda = 405 \text{ nm}$ and $P = 1.352 \text{ mW mm}^{-2}$. Meanwhile, when the photodetector is exposed to the 1064 nm near-IR light with the same power density, relatively high responsivity ($R = 10 \text{ mA W}^{-1}$) and specific detectivity ($D^* = 3.5 \times 10^7 \text{ Jones}$) can be obtained. These parameters are significant, even in comparison with other outstanding photodetectors fabricated on ternary compounds [29-34] or quasi-1D wires [29, 30, 35, 36]. Considering the broadband photoresponse, the advantage of $\text{Ta}_2\text{Ni}_3\text{Se}_8$ photodetector is more prominent.

The dependence of optoelectronic properties on laser power density is further studied. Considering the harmless feature of visible light, the 635 nm laser is selected to perform more measurements. As shown in figure 4(a), the I - V curves exhibit a clear dependence on power density. The photocurrent is calculated and plotted as a function of bias voltage for different power densities ranging from 0.16 to 1.352 mW mm^{-2} (figure 4(b)). Two characteristics can be observed. First, the photocurrent increases as the power density increases. Second, all the curves are near linear, which is easy to understand because of the linear dependence of the curves in figure 4(a). The inset of figure 4(b) shows the time-resolved photocurrent taken under different power densities and 0.01 V bias. The ladder-like curve shows well-defined ON and OFF states, indicating good stability and nonvolatile feature of the device. The photocurrent is about 9 nA at 1.352 mW mm^{-2} and decreases to 1 nA at 0.16 mW mm^{-2} . Upon further decreasing the power density, no obvious photocurrent is detected. Additional experiments performed to test the long-term stability can be found in the supplementary information.

The relationship between photocurrent and power density is important for studying the

underlying mechanism [7, 30, 31]. Generally, the photocurrent is a power function of the power density, i.e., $I_{\text{ph}} \propto P^\alpha$, where α is the power exponent. It is suggested that $\alpha = 1$ corresponds to the ideal photoconductive (PC) effect and $\alpha < 1$ indicates existence of photogating effect arising from trapping states [31]. Figure 4(c) shows the photocurrent plotted as a function of power density at 0.1 V, 0.3 V and 0.5 V biases. The data points are fitted to the power law, which give α values of 1.14, 1.16 and 1.14, respectively. These values appear to be independent of bias, which is consistent with the linear photocurrent-bias relationship mentioned above (figure 4(b)). The consistent values also confirm the reliability of the fits. Unexpectedly, α here is larger than 1, which suggests another mechanism than the photoconductive or photogating effect. Usually, α over 1 is related to photo-bolometric effect [37, 38]. Since the laser spot covers the entire channel area, the channel of the photodetector is heated evenly. That is, thermal gradients are negligible and thermoelectric mechanism can be ruled out. The generation of photocurrent is simply attributed to the decrease in channel resistance caused by heating due to photon absorption (see figure 5(a) for a schematic illustration of this effect). In addition to the power-law fits, more evidence can support the determination of the photo-bolometric effect. First, this effect requires, in principle, that the photocurrent is linearly proportional to the bias voltage. This is consistent with our measurements (figure 4(b)). Second, the photo-bolometric effect leads to a gradual increase in the responsivity and detectivity [37]. This can also be seen in our case, as shown in figure 4(d). The responsivity here can be formulated as $R = \frac{I_{\text{ph}}}{P_S} \propto \frac{P^\alpha}{P_S} \propto P^{0.14}$. It is thus reasonable that the responsivity increases with increasing power density and gradually approaches saturation. Third, this effect does not involve the bandgap width [7]. Therefore, a broadband photoresponse is expected. This is exactly the most important feature of $\text{Ta}_2\text{Ni}_3\text{Se}_8$ photodetectors. All these facts are self-consistent and demonstrate the dominant role of the photo-bolometric effect.

Furthermore, the response time of the $\text{Ta}_2\text{Ni}_3\text{Se}_8$ photodetector is studied in detail. Figures 5(b)-(i) show the time-resolved photocurrent taken at 0.01 V bias and $P = 1.352$

mW mm⁻² under periodic illumination of different wavelengths (405-1064 nm). All curves exhibit good switching cycle stability, indicating that the photodetector can operate well and persistently at various wavelengths. As a commonly used method, the rising time (τ_{rise}) is defined as the time for the photocurrent to increase from 10% to 90% of the maximum value, and the recovery time (τ_{decay}) is the time for the photocurrent to decrease from 90% to 10%. As shown in the insets of figures 5(b)-(i), the determination process gives relatively short response time ($\tau_{\text{rise}} < 600$ ms and $\tau_{\text{decay}} < 820$ ms) in the detection spectral range, which is comparable to the performance of some benchmark photodetectors reported previously, such as monolayer MoS₂ [39], Ta₂Se₈I [37], SnSe [40] and graphene oxide [41]. The fastest response occurs under 830 nm illumination, i.e., $\tau_{\text{rise}} = 360$ ms and $\tau_{\text{decay}} = 400$ ms. In addition, the good square waveforms indicate that the devices are not RC constant limited for the given parameters. See the supplementary information for the relationship between the RC constant and the photocurrent-time waveform and the power density dependence of the response time.

Given the prominent performance and the broadband photoresponse, it is natural to extend the testing further into longer wavelength region, such as the telecommunication band, which is important for today's industrial and consumer electronics [3, 42]. Here we select two typical wavelengths in the telecommunication band, namely O band 1310 nm and C band 1550 nm for testing. Figure 6(a) presents a schematic illustration of the Ta₂Ni₃Se₈ photodetector under global telecommunication wavelength illumination. As shown in figure 6(b), linear I - V curves together with clear photoresponse are again observed. Figures 6(c) and (d) show the time-resolved photocurrent at 0.01 V bias under periodic radiation of 1310 nm and 1550 nm, respectively. The device again exhibits good stability and durability. In the meanwhile, the response is also fast, represented by short response time, namely $\tau_{\text{rise}} = 430$ ms and $\tau_{\text{decay}} = 414$ ms for 1310 nm and $\tau_{\text{rise}} = 354$ ms and $\tau_{\text{decay}} = 345$ ms for 1550 nm. These values are shorter than the response time of other IR materials, including Ta₂NiSe₅ [43], VO₂ [44] and Ta₂Se₈I [37]. This result is of great

significance because the pronounced response to 1310 nm and 1550 nm suggests promising applications in optical communications and fiber optic cable testing in O band and C band. To further highlight the performance of Ta₂Ni₃Se₈ as a broadband photodetector, a detailed comparison with other reported materials is listed in Table 1. Considering the quasi-1D layered feature in its structure, the potential to build nanodevices on Ta₂Ni₃Se₈ makes it even more important in future electronic and optoelectronic applications.

4. Conclusion

In conclusion, we have synthesized high-quality Ta₂Ni₃Se₈ crystals and fabricated photodetectors on the wire samples. The photodetector exhibits relatively high photoresponsivity (10 mA W⁻¹) and specific detectivity ($D^* = 3.5 \times 10^7$ Jones) and comparably short response time ($\tau_{\text{rise}} = 433$ ms, $\tau_{\text{decay}} = 372$ ms) for $\lambda = 1064$ nm, 0.5 V bias and $P = 1.352$ mW mm⁻². Through extensive measurement and analysis, it is determined that the dominant mechanism for photocurrent generation is the photo-bolometric effect. This effect is believed to be responsible for the very broad spectral detection capability, extending into the mid- to long-IR region. More importantly, the pronounced response to 1310 nm and 1550 nm wavelengths manifests its promising applications in optical communications. Future work can focus on the quantum confinement effects at the nanoscale, such as optimizing the optoelectronic properties by manufacturing nanodevices and applying gating techniques.

Acknowledgments

This work was supported by the National Key R&D Program of China (Grant No. 2021YFA1600201), the National Natural Science Foundation of China (Grant Nos. 11874363, 11974356 and U1932216) and Anhui Province Laboratory of High Magnetic Field (Grant No. AHHM-FX-2020-01).

Data availability statement

All data that support the findings of this study are included within the article (and any supplementary files).

References

- [1] Hu X, Zhang X, Liang L, Bao J, Li S, Yang W and Xie Y 2014 High-Performance Flexible Broadband Photodetector Based on Organolead Halide Perovskite *Advanced Functional Materials* **24** 7373-80
- [2] Deng H, Yang X, Dong D, Li B, Yang D, Yuan S, Qiao K, Cheng Y B, Tang J and Song H 2015 Flexible and Semitransparent Organolead Triiodide Perovskite Network Photodetector Arrays with High Stability *Nano Lett* **15** 7963-9
- [3] Xiao P, Mao J, Ding K, Luo W, Hu W, Zhang X, Zhang X and Jie J 2018 Solution-Processed 3D RGO-MoS₂ /Pyramid Si Heterojunction for Ultrahigh Detectivity and Ultra-Broadband Photodetection *Adv Mater* **30** 1801729
- [4] Yuan H, Liu X, Afshinmanesh F, Li W, Xu G, Sun J, Lian B, Curto A G, Ye G, Hikita Y, Shen Z, Zhang S C, Chen X, Brongersma M, Hwang H Y and Cui Y 2015 Polarization-sensitive broadband photodetector using a black phosphorus vertical p-n junction *Nat Nanotechnol* **10** 707-13
- [5] Chen R, Ng K W, Ko W S, Parekh D, Lu F, Tran T T, Li K and Chang-Hasnain C 2014 Nanophotonic integrated circuits from nanoresonators grown on silicon *Nat Commun* **5** 4325
- [6] Kim I, Martins R J, Jang J, Badloe T, Khadir S, Jung H Y, Kim H, Kim J, Genevet P and Rho J 2021 Nanophotonics for light detection and ranging technology *Nat Nanotechnol* **16** 508-24
- [7] You J, Luo Y, Yang J, Zhang J, Yin K, Wei K, Zheng X and Jiang T 2020 Hybrid/Integrated Silicon Photonics Based on 2D Materials in Optical Communication Nanosystems *Laser & Photonics Reviews* **14** 2000239
- [8] Chen H, Liu H, Zhang Z, Hu K and Fang X 2016 Nanostructured Photodetectors: From Ultraviolet to Terahertz *Adv Mater* **28** 403-33
- [9] Kung P, Zhang X, Walker D, Saxler A, Piotrowski J, Rogalski A and Razeghi M 1995 Kinetics of photoconductivity in n - type GaN photodetector *Applied Physics Letters* **67** 3792-4
- [10] Huang Z, Carey J E, Liu M, Guo X, Mazur E and Campbell J C 2006 Microstructured silicon photodetector *Applied Physics Letters* **89** 033506
- [11] Piccardo M, Rubin N A, Meadowcroft L, Chevalier P, Yuan H, Kimchi J and Capasso F 2018 Mid-infrared two-photon absorption in an extended-wavelength InGaAs photodetector *Applied Physics Letters* **112** 041106
- [12] Rogalski A 2005 HgCdTe infrared detector material: history, status and outlook *Reports on Progress in Physics* **68** 2267-336
- [13] Jia B W, Tan K H, Loke W K, Wicaksono S, Lee K H and Yoon S F 2018 Monolithic Integration of InSb Photodetector on Silicon for Mid-Infrared Silicon Photonics *ACS Photonics* **5** 1512-20
- [14] Ren D, Azizur-Rahman K M, Rong Z, Juang B C, Somasundaram S, Shahili M, Farrell A C, Williams B S and Huffaker D L 2019 Room-Temperature Midwavelength Infrared InAsSb Nanowire Photodetector Arrays with Al₂O₃ Passivation *Nano Lett* **19** 2793-802
- [15] Wang Q, Li C Z, Ge S, Li J G, Lu W, Lai J, Liu X, Ma J, Yu D P, Liao Z M and Sun D 2017 Ultrafast

- Broadband Photodetectors Based on Three-Dimensional Dirac Semimetal Cd₃As₂ *Nano Lett* **17** 834-41
- [16] Dai M, Wang C, Ye M, Zhu S, Han S, Sun F, Chen W, Jin Y, Chua Y and Wang Q J 2022 High-Performance, Polarization-Sensitive, Long-Wave Infrared Photodetection via Photothermoelectric Effect with Asymmetric van der Waals Contacts *ACS Nano* **16** 295-305
- [17] Zhang Q, Liu C, Liu X, Liu J, Cui Z, Zhang Y, Yang L, Zhao Y, Xu T T, Chen Y, Wei J, Mao Z and Li D 2018 Thermal Transport in Quasi-1D van der Waals Crystal Ta₂Pd₃Se₈ Nanowires: Size and Length Dependence *ACS Nano* **12** 2634-42
- [18] Liu X, Liu J, Antipina L Y, Hu J, Yue C, Sanchez A M, Sorokin P B, Mao Z and Wei J 2016 Direct Fabrication of Functional Ultrathin Single-Crystal Nanowires from Quasi-One-Dimensional van der Waals Crystals *Nano Lett* **16** 6188-95
- [19] Jeong B J, Choi K H, Jeon J, Yoon S O, Chung Y K, Sung D, Chae S, Kim B J, Oh S, Lee S H, Woo C, Kim T Y, Ahn J, Lee J H, Huh J, Yu H K and Choi J Y 2021 Ternary Transition Metal Chalcogenide Nb₂Pd₃Se₈: A New Candidate of 1D Van der Waals Materials for Field - Effect Transistors *Advanced Functional Materials* **32** 2108104
- [20] Choi K H, Jeong B J, Jeon J, Chung Y K, Sung D, Yoon S O, Chae S, Kim B J, Oh S, Lee S H, Woo C, Dong X, Ghulam A, Ali J, Kim T Y, Seo M, Lee J H, Huh J, Yu H K and Choi J Y 2021 Ta₂ Ni₃ Se₈ : 1D van der Waals Material with Ambipolar Behavior *Small* **17** e2102602
- [21] Liu X, Liu S, Antipina L Y, Zhu Y, Ning J, Liu J, Yue C, Joshy A, Zhu Y, Sun J, Sanchez A M, Sorokin P B, Mao Z, Xiong Q and Wei J 2020 High yield production of ultrathin fibroid semiconducting nanowire of Ta₂Pd₃Se₈ *Nano Research* **13** 1627-35
- [22] Wang T, Zhu Y, Mao Z and Xu Y-Q 2021 Tunneling Effects in Crossed Ta₂Pt₃Se₈–Ta₂Pd₃Se₈ Nanowire Junctions: Implications for Anisotropic Photodetectors *ACS Applied Nano Materials* **4** 1817-24
- [23] Blaha P, Schwarz K, Sorantin P and Trickey S B 1990 Full-potential, linearized augmented plane wave programs for crystalline systems *Computer Physics Communications* **59** 399-415
- [24] Perdew J P, Burke K and Ernzerhof M 1996 Generalized Gradient Approximation Made Simple *Physical Review Letters* **77** 3865-8
- [25] Oh S, Jeon J, Choi K H, Chae S, Park J-H, Lee J-H, Yu H K and Choi J-Y 2022 Synthesis of one-dimensional van der Waals material alloys *Applied Physics Letters* **120** 061903
- [26] Zhang B Y, Liu T, Meng B, Li X, Liang G, Hu X and Wang Q J 2013 Broadband high photoresponse from pure monolayer graphene photodetector *Nat Commun* **4** 1811
- [27] Weng S R, Zhen W L, Yan X, Yue Z L, Hu H J, Xu F, Zhang R R, Pi L, Zhu W K and Zhang C J 2021 Wide-spectrum photodetector constructed on a centimeter-scale flexible SnSe₂ film using a new one-step strategy *J Phys Condens Matter* **33** 395001
- [28] Hu L, Yan J, Liao M, Wu L and Fang X 2011 Ultrahigh external quantum efficiency from thin SnO₂ nanowire ultraviolet photodetectors *Small* **7** 1012-7
- [29] Yan X, Zhen W-L, Hu H-J, Pi L, Zhang C-J and Zhu W-K 2021 High-Performance Visible Light Photodetector Based on BiSeI Single Crystal *Chinese Physics Letters* **38** 068103
- [30] Hu H J, Zhen W L, Weng S R, Li Y D, Niu R, Yue Z L, Xu F, Pi L, Zhang C J and Zhu W K 2022 Enhanced optoelectronic performance and photogating effect in quasi-one-dimensional BiSeI wires *under*

review

- [31] Zhen W, Zhou X, Weng S, Zhu W and Zhang C 2022 Ultrasensitive, Ultrafast, and Gate-Tunable Two-Dimensional Photodetectors in Ternary Rhombohedral ZnIn₂S₄ for Optical Neural Networks *ACS Applied Materials & Interfaces* **14** 12571-82
- [32] Weng S, Zhen W, Li Y, Yan X, Han H, Huang H, Pi L, Zhu W, Li H and Zhang C 2020 Air-Stable Wide-Bandgap 2D Semiconductor ZnIn₂S₄ *physica status solidi (RRL) – Rapid Research Letters* **14** 2000085
- [33] Li L, Ye G, Luo T, Chen X, Zhang G, Wu H, Yang L, Zhang W and Chang H 2022 Centimeter-Sized Stable Zero-Dimensional Cs₃Bi₂I₉ Single Crystal for Mid-Infrared Lead-Free Perovskite Photodetector *The Journal of Physical Chemistry C* **126** 3646-52
- [34] Yang H, Tan C, Deng C, Zhang R, Zheng X, Zhang X, Hu Y, Guo X, Wang G, Jiang T, Zhang Y, Peng G, Peng H, Zhang X and Qin S 2019 Bolometric Effect in Bi₂O₂Se Photodetectors *Small* **15** 1904482
- [35] Mayorga-Martinez C C, Sofer Z, Luxa J, Huber S, Sedmidubsky D, Brazda P, Palatinus L, Mikulics M, Lazar P, Medlin R and Pumera M 2018 TaS₃ Nanofibers: Layered Trichalcogenide for High-Performance Electronic and Sensing Devices *ACS Nano* **12** 464-73
- [36] Mikulics M, Lu J G, Huang L, Tse P L, Zhang J Z, Mayer J and Hardtdegen H 2020 Laser micro annealing conditioning for the suppression of statistical scatter in freestanding Sb₂Te₃ nanowire resistance *FlatChem* **21** 100164
- [37] Cheng J, An C, Li L, Chen L, Cui Y, Yan Q, Yin Y, Zhou W, Peng Y, Wang W and Tang D 2021 High-performance near-infrared photodetector based on quasi one-dimensional layered (TaSe₄)₂ *Applied Physics Letters* **119** 201909
- [38] Yin C, Gong C, Chu J, Wang X, Yan C, Qian S, Wang Y, Rao G, Wang H, Liu Y, Wang X, Wang J, Hu W, Li C and Xiong J 2020 Ultrabroadband Photodetectors up to 10.6 microm Based on 2D Fe₃O₄ Nanosheets *Adv Mater* **32** 2002237
- [39] Konstantatos G, Badioli M, Gaudreau L, Osmond J, Bernechea M, Garcia de Arquer F P, Gatti F and Koppens F H 2012 Hybrid graphene-quantum dot phototransistors with ultrahigh gain *Nat Nanotechnol* **7** 363-8
- [40] Hao L, Du Y, Wang Z, Wu Y, Xu H, Dong S, Liu H, Liu Y, Xue Q, Han Z, Yan K and Dong M 2020 Wafer-size growth of 2D layered SnSe films for UV-Visible-NIR photodetector arrays with high responsivity *Nanoscale* **12** 7358-65
- [41] Cao Y, Yang H, Zhao Y, Zhang Y, Ren T, Jin B, He J and Sun J-L 2017 Fully Suspended Reduced Graphene Oxide Photodetector with Annealing Temperature-Dependent Broad Spectral Binary Photoresponses *ACS Photonics* **4** 2797-806
- [42] Wu E, Wu D, Jia C, Wang Y, Yuan H, Zeng L, Xu T, Shi Z, Tian Y and Li X 2019 In Situ Fabrication of 2D WS₂/Si Type-II Heterojunction for Self-Powered Broadband Photodetector with Response up to Mid-Infrared *ACS Photonics* **6** 565-72
- [43] Li L, Wang W, Gan L, Zhou N, Zhu X, Zhang Q, Li H, Tian M and Zhai T 2016 Ternary Ta₂NiSe₅ Flakes for a High - Performance Infrared Photodetector *Advanced Functional Materials* **26** 8281-9
- [44] Zhou X, Zhao L, Zhen W, Lin Y, Wang C, Pan T, Li L, Du G, Lu L, Cao X and Li D 2021 Phase - Transition - Induced VO₂ Thin Film IR Photodetector and Threshold Switching Selector for Optical Neural Network Applications *Advanced Electronic Materials* **7** 2001254

- [45] Buscema M, Groenendijk D J, Blanter S I, Steele G A, van der Zant H S and Castellanos-Gomez A 2014 Fast and broadband photoresponse of few-layer black phosphorus field-effect transistors *Nano Lett* **14** 3347-52
- [46] Choi W, Cho M Y, Konar A, Lee J H, Cha G B, Hong S C, Kim S, Kim J, Jena D, Joo J and Kim S 2012 High-detectivity multilayer MoS₂ phototransistors with spectral response from ultraviolet to infrared *Adv Mater* **24** 5832-6
- [47] Yang H, Cao Y, He J, Zhang Y, Jin B, Sun J-L, Wang Y and Zhao Z 2017 Highly conductive free-standing reduced graphene oxide thin films for fast photoelectric devices *Carbon* **115** 561-70
- [48] Xu T, Luo M, Shen N, Yu Y, Wang Z, Cui Z, Qin J, Liang F, Chen Y, Zhou Y, Zhong F, Peng M, Zubair M, Li N, Miao J, Lu W, Yu C and Hu W 2021 Ternary 2D Layered Material FePSe₃ and Near - Infrared Photodetector *Advanced Electronic Materials* **7** 2100207
- [49] Li Z, Li Z, Shi Z and Fang X 2020 Facet - Dependent, Fast Response, and Broadband Photodetector Based on Highly Stable All - Inorganic CsCu₂I₃ Single Crystal with 1D Electronic Structure *Advanced Functional Materials* **30** 2002634
- [50] Patel A, Limberkar C, Patel K, Bhakhar S, Patel K D, Solanki G K and Pathak V M 2021 Low temperature anisotropic photoresponse study of bulk ZrS₃ single crystal *Sensors and Actuators A: Physical* **331** 112969
- [51] Dixit V, Nair S, Joy J, Vyas C U, Solanki G K, Patel K D and Pathak V M 2018 Growth, characterization and photoconduction properties of Sb_{0.1}Mo_{0.9}Se₂ single crystals grown by DVT technique *Materials Science in Semiconductor Processing* **88** 1-9

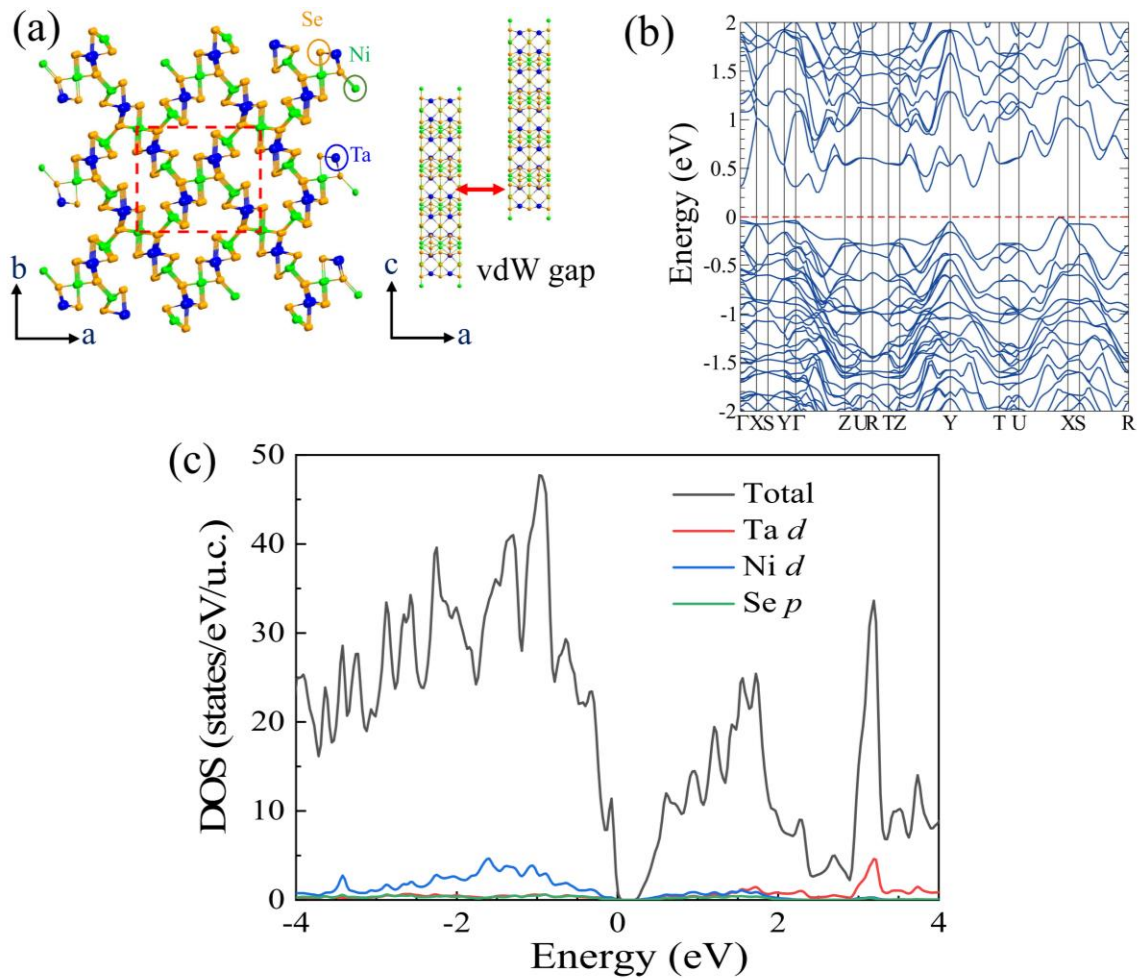


Figure 1. (a) Schematic crystal structure of Ta₂Ni₃Se₈. Blue, green and orange balls represent Ta, Ni, Se atoms, respectively. (b) Band structure along the high symmetry directions in the reciprocal space. (c) Total and partial density of states for Ta₂Ni₃Se₈. The Fermi energy is set at the valence band maximum.

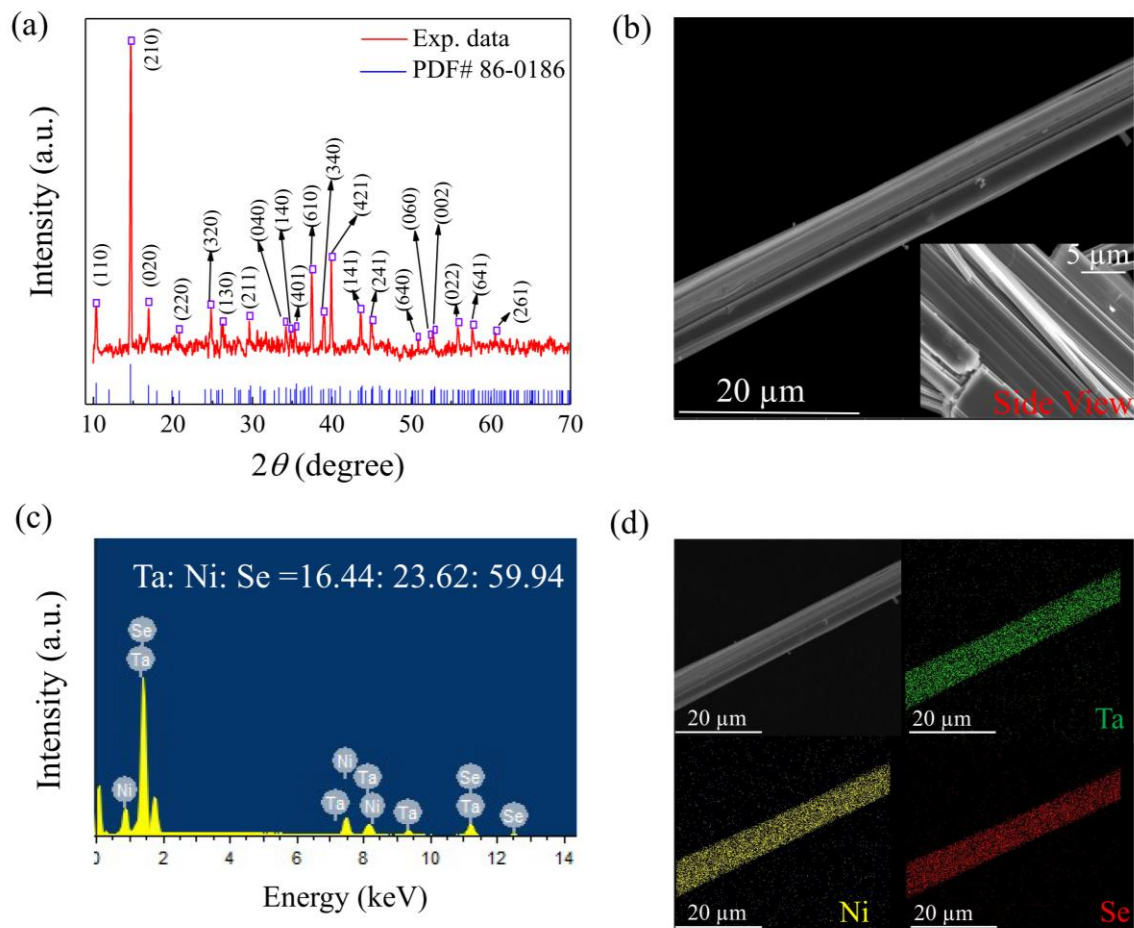


Figure 2. (a) XRD pattern of the as-grown $\text{Ta}_2\text{Ni}_3\text{Se}_8$ crystals. (b) SEM image of a $\text{Ta}_2\text{Ni}_3\text{Se}_8$ wire. Inset: SEM image of side view showing quasi-1D structure with layered texture. (c) EDS spectrum reveals the atomic ratio. (d) EDS elemental mapping taken on a $\text{Ta}_2\text{Ni}_3\text{Se}_8$ wire.

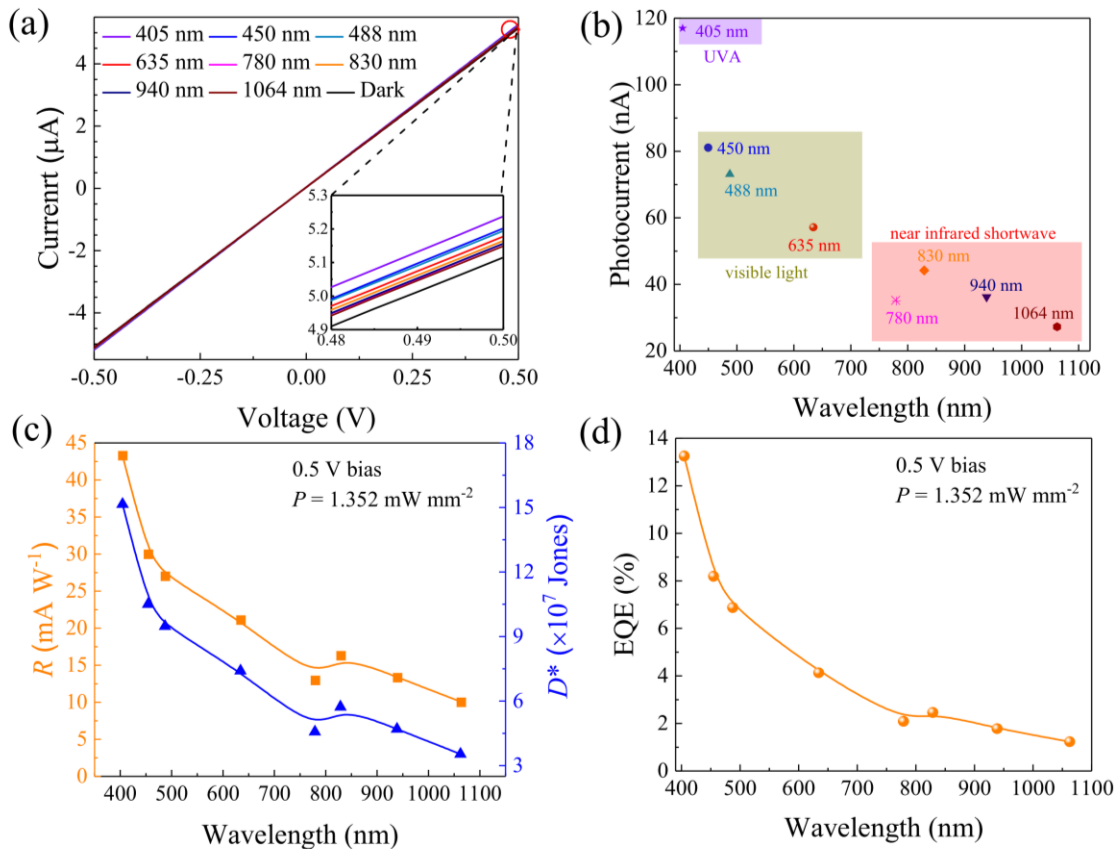


Figure 3. (a) *I-V* characteristic curves taken in the dark and under laser illumination of different wavelengths. Inset: an enlarged view of the *I-V* curves in the range of 0.48 V to 0.5 V. (b) Photocurrents for various wavelengths under 0.5 V bias. (c) Responsivity (left) and specific detectivity (right) and (d) EQE as a function of laser wavelength.

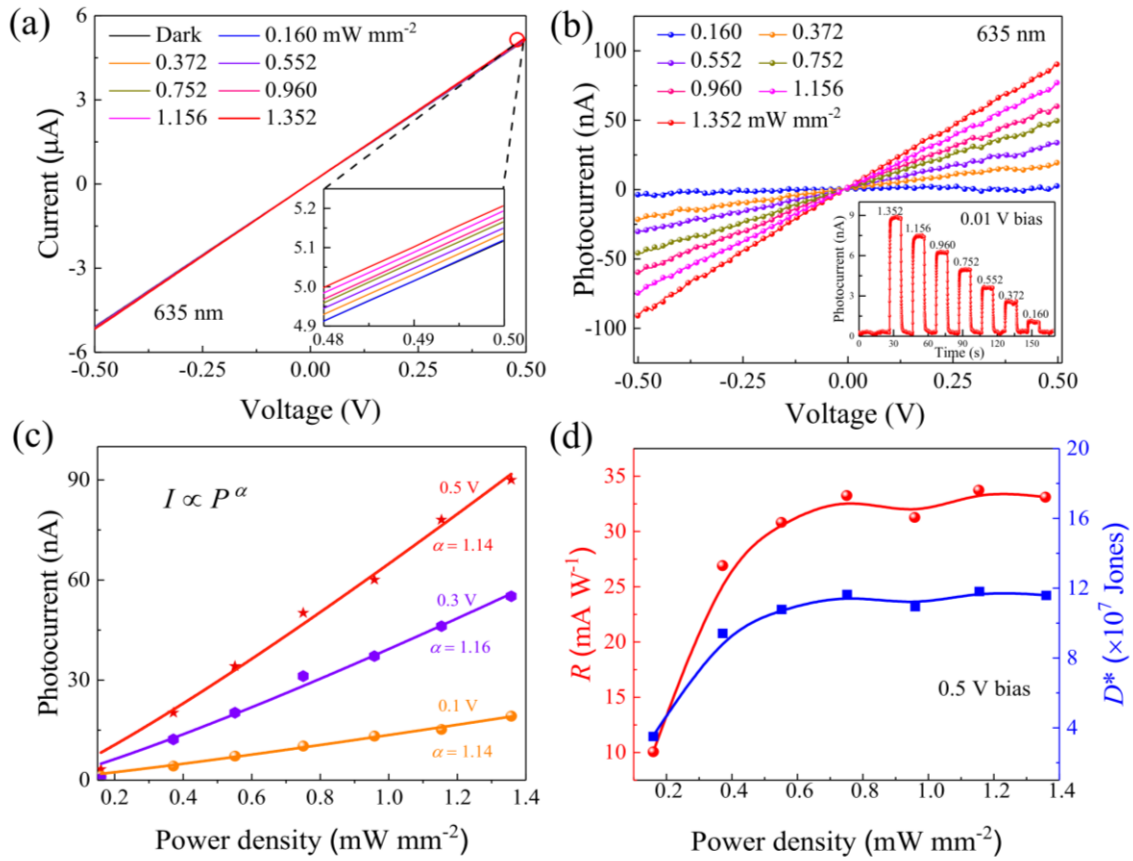


Figure 4. (a) I - V curves taken in the dark and under 635 nm laser tuned to different power densities. Inset: an enlarged view of the I - V curves in the range of 0.48 V to 0.5 V. (b) Photocurrent as a function of bias voltage for different laser power densities. Inset: Time-resolved photocurrent taken under different power densities and 0.01 V bias. (c) Photocurrent vs laser power density under 0.1 V, 0.3 V and 0.5 V biases. The curves represent the power-law fit. (d) Responsivity (left) and specific detectivity (right) as a function of laser power density. The curves are guides for eyes.

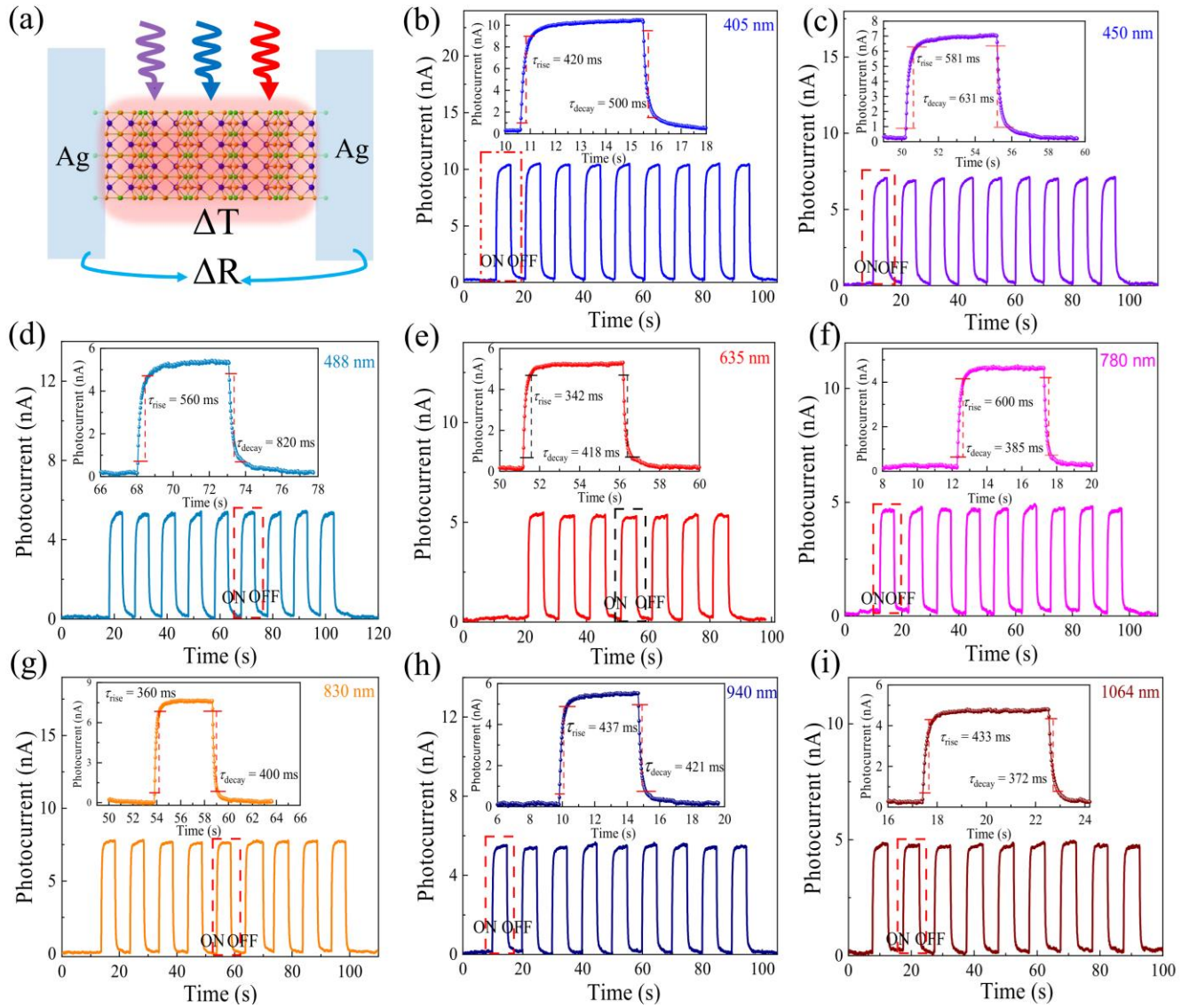


Figure 5. (a) Schematic illustration of the photo-bolometric effect. (b)-(i) Time-resolved photocurrent at 0.01 V bias and $P = 1.352 \text{ mW/mm}^2$ under periodic illumination of 405 nm, 450 nm, 488 nm, 635 nm, 780 nm, 830 nm, 940 nm and 1064 nm, respectively. Insets: A single ON-OFF cycle showing determination of response time.

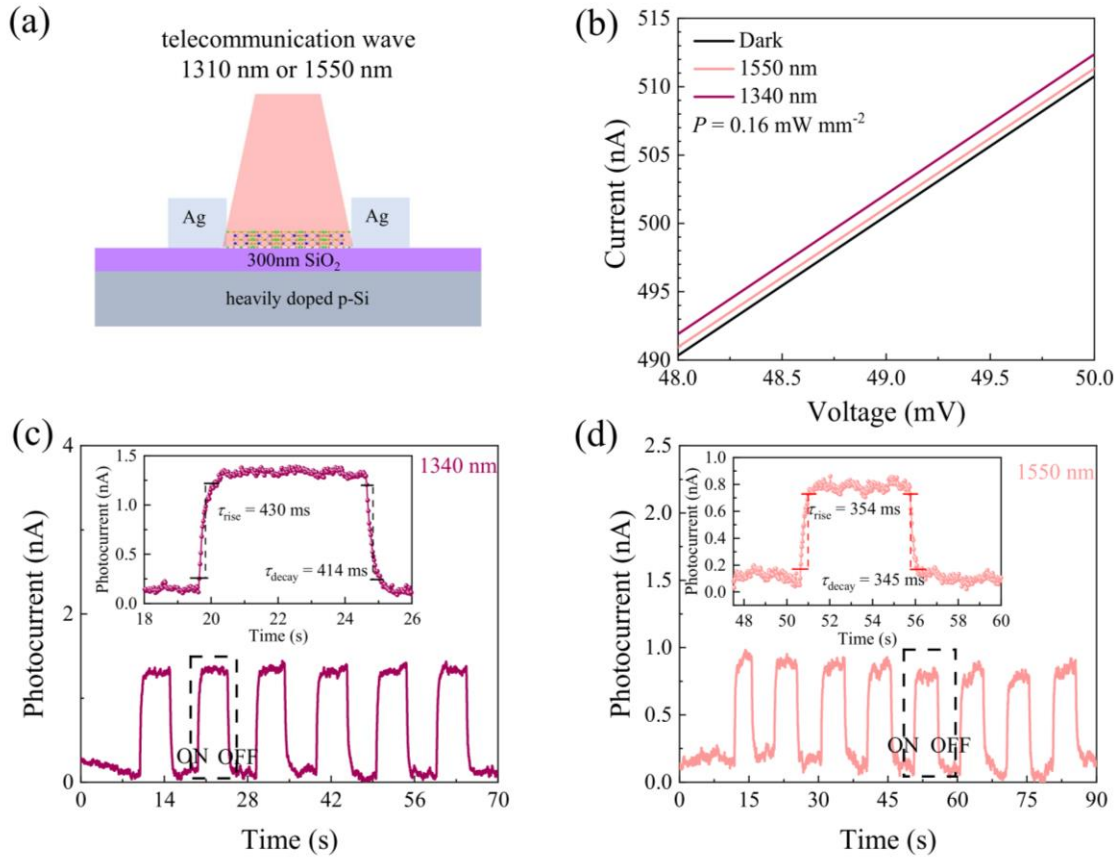


Figure 6. (a) Schematic illustration of Ta₂Ni₃Se₈ photodetector operating at 1310 nm or 1550 nm telecommunication wavelength. (b) I - V curves taken in the dark and at 1310 nm and 1550 nm wavelengths tuned to 0.16 mW mm⁻² in the range of 0.48 V to 0.5 V. (c) (d) Time-resolved photocurrent at 0.01 V bias and $P = 0.16$ mW mm⁻² under periodic radiation of 1310 nm and 1550 nm, respectively. Insets: A single ON-OFF cycle showing determination of response time.

Table 1. Comparison of performance parameters of typical broadband photodetectors.

Materials	Mechanism	Bias (V)	Detection range	R (mA W ⁻¹)	D^* ($\times 10^8$ Jones)	$\tau_{\text{rise}}/\tau_{\text{decay}}$ (ms)
BP flake [45]	PC	0.2	405-940 nm	4.8	-	$\sim 1/\sim 4$
MoS ₂ flake [46]	PC	0.1	455-850 nm	50-120	100-1000	>1000

RGO film [47]	PB	1.0	UV-THz	0.3-1.3	-	~135/~150
FePSe ₃ flake [48]	PC	0.1	450-940 nm	3.9	1.17	~180/~400
CsCu ₂ I ₃ bulk [49]	PC	10	300-700 nm	10-52	180-930	~0.2/~15
ZrS ₃ bulk [50]	PC	1.0	Visible light	0.12	64.3	1000/1800
MoSe ₂ bulk [51]	PC	1.0	400-700 nm	2.35	0.023	-
Cs ₃ Bi ₂ I ₉ bulk [33]	PC	1.0	343-4000 nm	< 0.59	< 1	~4000/~10000
Ta ₂ Ni ₃ Se ₈ bulk	PB	0.5	405-1550 nm	10-43.3	0.35-1.51	~400/~400
(this work)						

Supplementary information for

Broadband Photoresponse Arising from Photo-Bolometric Effect in Quasi-One-Dimensional $\text{Ta}_2\text{Ni}_3\text{Se}_8$

1. Optical image of $\text{Ta}_2\text{Ni}_3\text{Se}_8$ crystals, Raman and EDS data

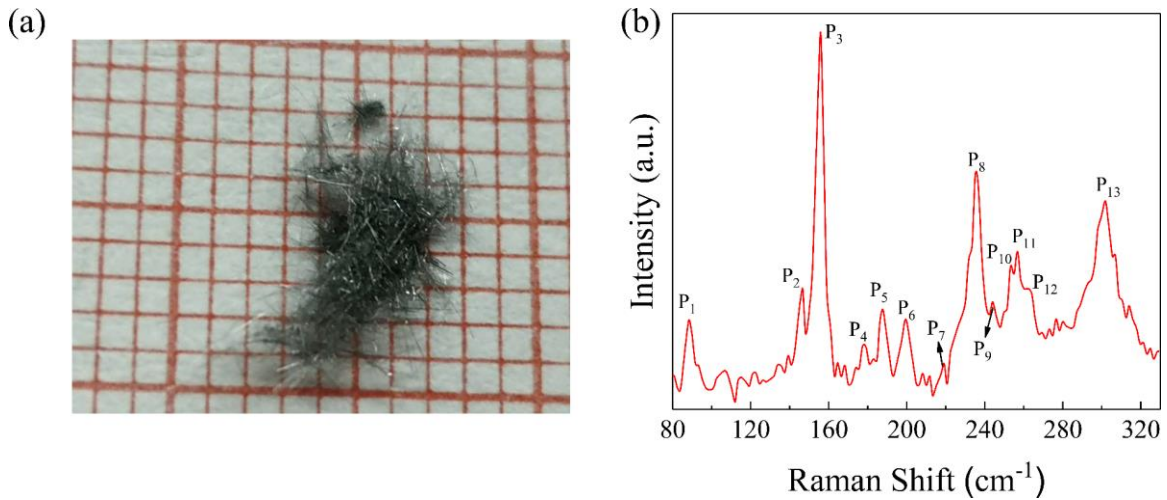


Figure S1. (a) An optical image of the as-grown $\text{Ta}_2\text{Ni}_3\text{Se}_8$ crystals. The size of each small grid is $1 \times 1 \text{ mm}^2$. (b) Raman spectrum of $\text{Ta}_2\text{Ni}_3\text{Se}_8$.

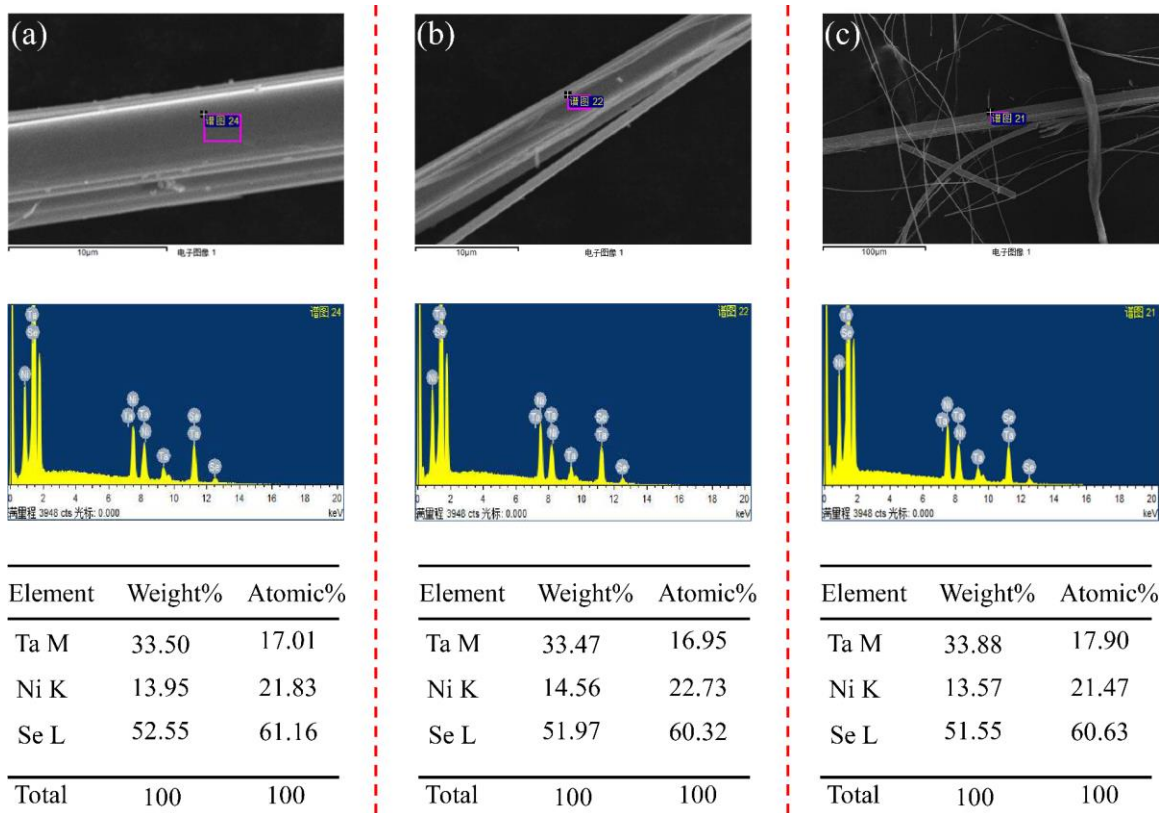


Figure S2. EDS data of different $\text{Ta}_2\text{Ni}_3\text{Se}_8$ crystals.

2. Optoelectronic measurements of devices D2 and D3

The optoelectronic properties of two additional devices, namely D2 and D3, were measured. The channel dimensions of D2 and D3 are approximately $1.5 \mu\text{m}$ (width) \times 2.4 mm (length) and $1.7 \mu\text{m}$ (width) \times 3 mm (length), respectively. Compared with the first device D1 with dimensions of $1 \mu\text{m}$ (width) \times 2 mm (length), these two devices reveal no significant differences. All of these devices exhibit a broadband photoresponse. The α values obtained from the power-law fits are also greater than 1, which indicates that the photocurrent generation mechanism of D2 and D3 is also the photo-bolometric effect.

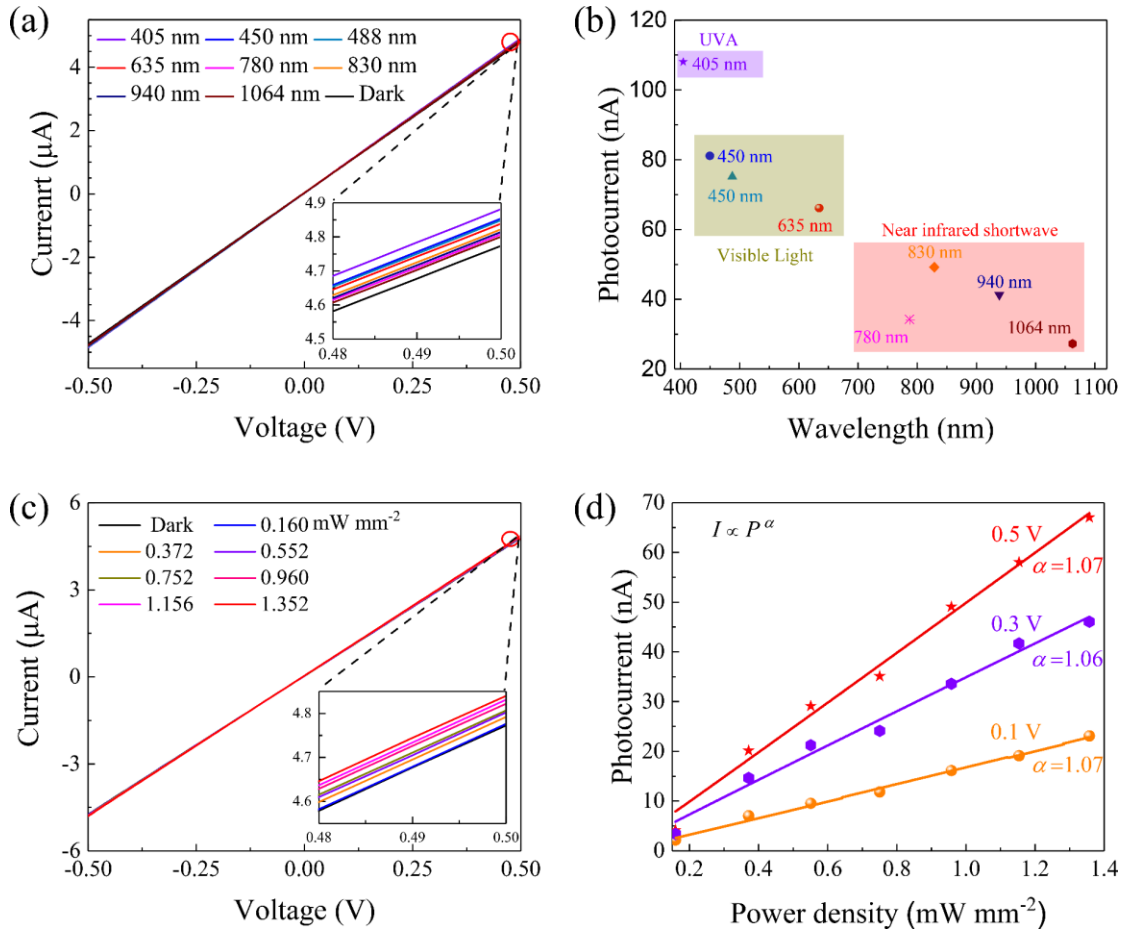


Figure S3. Optoelectronic measurements of device D2. (a) I - V characteristic curves taken in the dark and under laser illumination of different wavelengths. Inset: an enlarged view of the I - V curves in the range of 0.48 V to 0.5 V. (b) Photocurrents for various wavelengths under 0.5 V bias. (c) I - V curves taken in the dark and under 635 nm laser tuned to different power densities. Inset: an enlarged view of the I - V curves in the range of 0.48 V to 0.5 V. (d) Photocurrent vs laser power density under 0.1 V, 0.3V and 0.5 V biases. The curves represent the power-law fit.

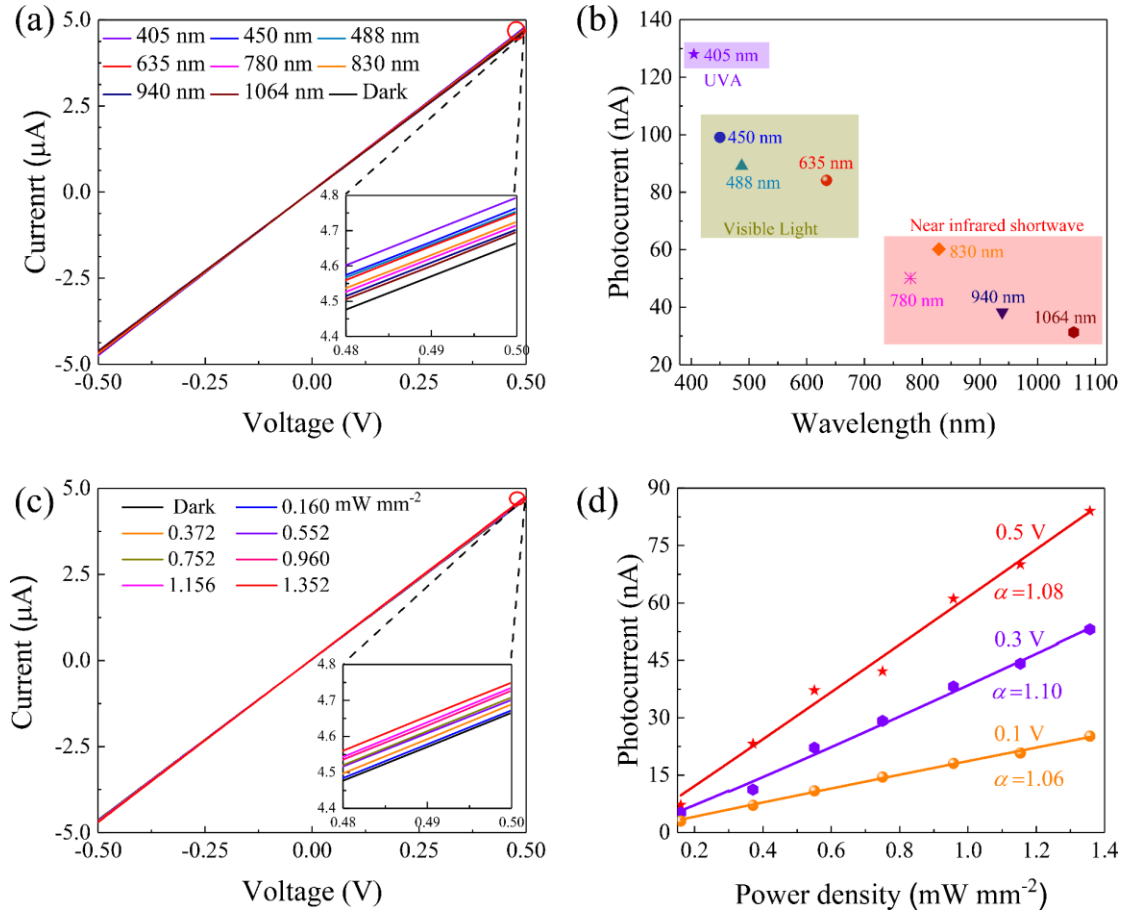


Figure S4. Optoelectronic measurements of device D3. (a) I - V characteristic curves taken in the dark and under laser illumination of different wavelengths. Inset: an enlarged view of the I - V curves in the range of 0.48 V to 0.5 V. (b) Photocurrents for various wavelengths under 0.5 V bias. (c) I - V curves taken in the dark and under 635 nm laser tuned to different power densities. Inset: an enlarged view of the I - V curves in the range of 0.48 V to 0.5 V. (d) Photocurrent vs laser power density under 0.1 V, 0.3V and 0.5 V biases. The curves represent the power-law fit.

3. Long-term stability

Additional experiments were performed to test the long-term stability. First, the device operated for 30 response cycles with repeated illumination on and off. In each cycle, the illumination on and off time was set to 10 s. The power density was set to a high value, i.e., 1.352 mW mm^{-2} . As shown in figure S5(a), the device exhibits high stability and

repeatability. Second, the device was tested under long time illumination (200 s). We can see that the stability of the device is also good enough in the long-term ON state. Once the illumination is turned off, the device can quickly return to the dark state, and the dark state is also stable after long-term operation. Combining the two tests, it is affirmed that the device has very good long-term stability and durability.

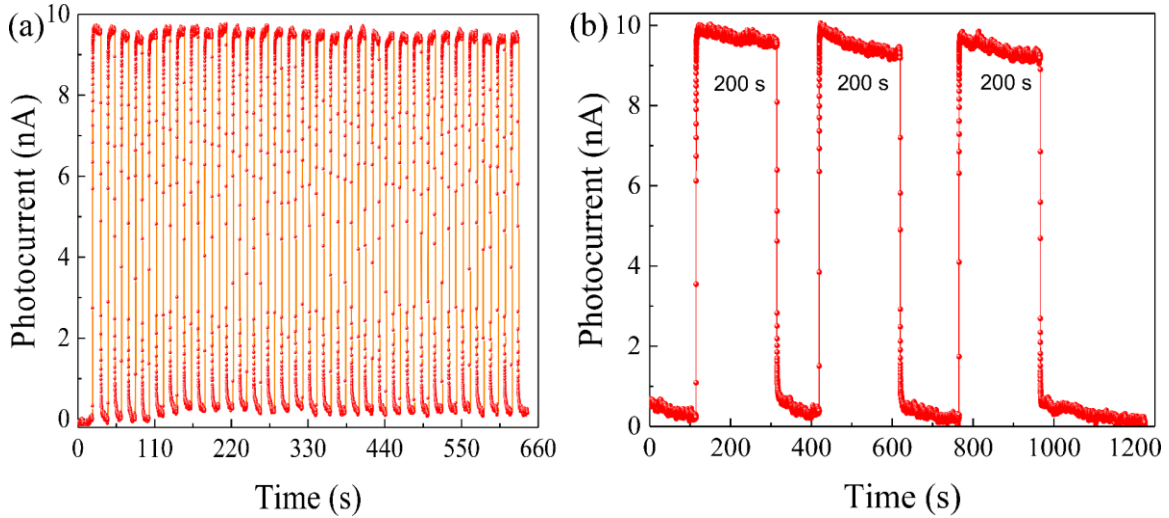


Figure S5. (a) 30 response cycles setting the power density to 1.352 mW mm^{-2} . (b) Stability of long illumination time (200 s). $\lambda = 635 \text{ nm}$ and $V_{\text{ds}} = 0.01 \text{ V}$.

4. RC constant and response time

The relationship between the RC constant and the photocurrent-time waveform is illustrated in figure S6. The response time of the device is limited by the RC constant, which usually occurs when the device is illuminated by high-frequency incident light, and the response time cannot keep up with the frequency of the light, resulting in distorted output waveform, as shown in figure S6(c). In this case, a large parasitic capacitance exists between the channel material and the contact electrodes [B. E. A. Saleh and M. C. Teich, *Fundamentals of Photonics*. (John Wiley & Sons, Inc., New York, Chichester, Brisbane, Toronto, Singapore, 1991).]. As seen in figures 3(a) and 4(a), the I - V curves of our devices show very good linearity, indicating that an ohmic contact is formed and the capacitance

is very small. Furthermore, in our experiments, the laser illumination is repeatedly turned on and off at a low frequency of 0.05 Hz (duty ratio: 50%). Figures 5(b)-5(i) show good switching cycle stability for all curves, indicating that the photodetector can work well and durably at various wavelengths. The slowest response appears at 488 nm, i.e., $\tau_{\text{rise}} = 560$ ms and $\tau_{\text{decay}} = 820$ ms, both of which are much shorter than the period of the incident light (20 s). The output waveforms are undistorted, similar to that in figure S6(b). These good square waveforms correspond to small parasitic capacitances, which is consistent with the linear I - V curves. That is, our devices are not RC constant limited for the given parameters.

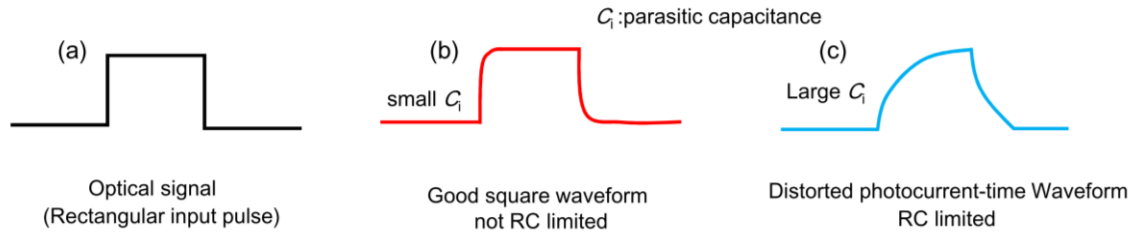


Figure S6. (a) Optical input signal, (b) output waveform not limited by RC constant and (c) output waveform limited by RC constant.

5. Power density dependence of response time

The power density dependence of the response time was investigated. As shown in figure S7, the response time is $\tau_{\text{rise}} = 342$ ms and $\tau_{\text{decay}} = 418$ ms for $P = 1.352$ mW mm⁻², $\tau_{\text{rise}} = 320$ ms and $\tau_{\text{decay}} = 360$ ms for $P = 0.75$ mW mm⁻², and $\tau_{\text{rise}} = 216$ ms and $\tau_{\text{decay}} = 327$ ms for $P = 1.352$ mW mm⁻², respectively. It seems that the response becomes slower at higher power densities. Here is a possible explanation. Given that the response time is not limited by the RC constant, another factor limiting the response time is the carrier transit time τ_{tr} , which is defined as the time the carriers take to go through the channel. It can be expressed as $\tau_{\text{tr}} = L^2 / 2\mu V_{\text{bias}}$, where L is the channel length and μ is the carrier mobility. As μ decreases, τ_{tr} and response time increase. For photodetectors conforming to the photo-bolometric effect, the heating process caused by photon absorption affects the carrier

mobility. For higher power densities, more light absorption means increased temperature and enhanced phonon scattering, which will suppress the carrier mobility. Therefore, higher power density corresponds to slower response.

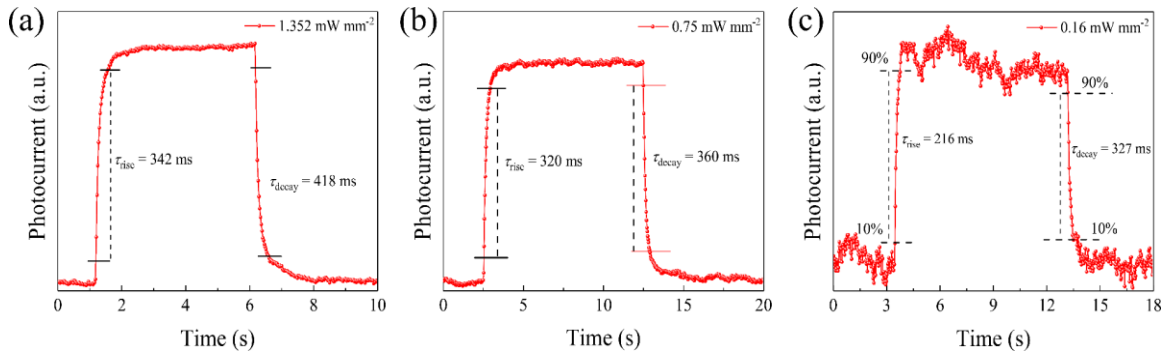


Figure S7. Response time measured under different power densities.